

Computing stationary free-surface shapes in microfluidics

By MICHAEL SCHINDLER, PETER TALKNER
AND PETER HÄNGGI

Institut für Physik, Universitätsstraße 1, 86159 Augsburg, Germany

(Received ?? and in revised form ??)

We propose a Finite-Element algorithm to compute free capillary surface shapes that are significantly deformed. The algorithm is thoroughly explained by physical as well as mathematical arguments. We show that it is robust in the sense that it yields the correct surface shape starting with quite different ones, without the need for re-meshing at the boundary. The errors of the computed shape's curvature are shown to be extremely small, at least an order of magnitude less than one percent in two accuracy tests. Our variational approach, formulated in arbitrary curved coordinates allows to substantiate the numerical observation that only a second-order approximation suffices for the free surface discretisation. Finally, we present a comparison of our numerical results with an experimentally observed droplet.

1. Introduction

The ability to transport and manipulate fluids on the micrometer scale has triggered a wide range of scientific investigations, as well as the development of many microfluidic devices (Squires & Quake 2005; Stone *et al.* 2004; Thiele 2003; Stone & Kim 2001). A very promising and unconventional way to agitate small amounts of liquid has recently been published by Wixforth *et al.* (2004), where tiny earthquakes (so-called surface-acoustic waves, SAW) are generated on a flat piezoelectric chip. When a SAW hits a small droplet an internal streaming pattern is induced by the *acoustic streaming effect* (Nyborg 1965). Moreover, the droplet becomes deformed and, depending on the strength of the SAW, stays pinned, or starts to move as a whole. In these experiments the droplet's diameter ranges from some $10\ \mu\text{m}$ to 1 mm. Its contact area with the flat substrate is well defined by prescribed wetting properties providing virtual pinning-beds to keep its motion confined.

These systems have recently been used for mixing smallest amounts of liquid, for aligning carbon nanotubes on surfaces and even for separating particles suspended in the fluid (Sritharan *et al.* 2005; Strobl *et al.* 2004, 2005; Guttenberg *et al.* 2004; Kostur *et al.* 2005). With the growing possibilities of such experimental setups involving free surfaces there is also a growing need for numerical algorithms that can predict the precise internal flow pattern and pressure field. This is essential not only for understanding the actuation mechanism and for optimising chip-layouts but also for estimating the shear rates of a flow and its mixing and transport properties.

For this purpose we develop a robust Finite-Element algorithm yielding very precise results in test examples. We also perform a comparison with an experimentally observed strong deformation of a droplet.

In §2 the mathematical formulation of the problem is presented in terms of differential equations is given together with the boundary conditions and the relevant parameter

regime. In §3 these equations and their boundary conditions are established by variational techniques. For the free-surface boundary condition we introduce a differential-geometric notation which allows to write it in a weak form. Section 5 then introduces the discrete implementation of the boundary conditions. In §6 we provide two examples that show the accuracy of the algorithm and two additional physical examples. Mathematical details are deferred into the appendices A–D.

2. Micro-flows with a free surface: Statement of the problem

We shall write all equations in tensor notation for arbitrary curvilinear coordinate systems. This will considerably simplify the differential geometric notation in the following sections. For the formulation of the full Navier–Stokes equations in curvilinear coordinates we refer to Aris (1989) and Luo & Bewley (2004). We use g_{ij} for the metric tensor of the underlying coordinate system, and an index that is preceded by a comma for denoting a covariant derivative. An repeated index that occurs in co- and contravariant positions is summed over.

2.1. The basic equations

We study incompressible and stationary flows, that are characterised by a small Reynolds number $Re = \rho \bar{x} \bar{v} / \eta$. Here, ρ is the density of the fluid, η its shear viscosity, and \bar{x} and \bar{v} denote typical magnitudes of length and velocity. Under these conditions the pressure field p and the velocity field with components v^i satisfy the Stokes equations (Landau & Lifschitz 1966)

$$v_{,i}^i = 0 \quad (2.1)$$

$$0 = \sigma_{,j}^{ij} + f^i \quad \text{with} \quad \sigma_{ij} = -pg_{ij} + \eta(v_{i,j} + v_{j,i}), \quad (2.2)$$

where σ_{ij} is the fluidic stress tensor, f^i an external force causing non-trivial streaming and pressure patterns within a domain V . This domain may be bounded by rigid walls and by free surfaces, as e.g. a droplet sitting on a substrate. Equations (2.1) and (2.2) then are subject to boundary conditions at the different parts of the boundary ∂V : First, the flow has to meet the *kinematic* boundary condition, requiring that the normal projection of a stationary velocity field vanishes there, i.e.,

$$v_i N^i = 0. \quad (2.3)$$

At rigid walls we will use the *no-slip* boundary condition, according to which the velocity vanishes also in the tangential directions of the boundary, implying

$$v_i T_\alpha^i = 0 \quad \text{for all } \alpha, \quad (2.4)$$

where T_α^i denotes the i th component of the tangential vector \mathbf{T}_α ($\alpha = 1, 2$). The remaining boundary is a free surface that dynamically adjusts its position such that the stress balance holds,

$$\sigma^{ij} N_j = \gamma \kappa N^i + T_\alpha^i \nabla_\alpha \gamma, \quad (2.5)$$

with the surface tension γ and the curvature κ . The last term denotes the tangent vector that is proportional to the gradient of the surface tension (see equation (C 5) in appendix C for a formal definition).

Equations (2.1)–(2.5) have been simplified by assuming that the fluid in domain V is surrounded by a medium of much smaller shear viscosity, which is the case e.g. for a water–air interface at room temperature. Therefore, the surrounding’s viscous stress contribution does not show up in the balance equation (2.5). We further assume that the

ambient pressure p_0 is homogeneous. Because the pressure is determined by the Stokes equations only up to a constant, we can split it into a part p_1 with vanishing average and use the ambient pressure p_0 as a homogeneous offset parameter which enters in equation (2.5)

$$p(\mathbf{x}) = p_0 + p_1(\mathbf{x}) \quad \text{with} \quad \int_V p_1 = 0. \quad (2.6)$$

2.2. The parameter regime

By transforming both, the bulk equation (2.2) and the free boundary condition (2.5) into dimensionless form in viscosity-scaling, one observes that the system may be characterised by two relevant ratios of forces, given by the dimensionless numbers

$$Bo = \frac{\bar{f}_c \bar{x}^2}{\gamma} \quad \text{and} \quad Ca = \frac{\eta \bar{v}}{\gamma}. \quad (2.7)$$

Here, \bar{x} , \bar{v} and \bar{f}_c denote typical magnitudes of length, velocity and the conservative part of the force density, respectively. Bo is a generalisation of the *Bond number* which is usually defined in terms of gravitational forces only. The *capillary number* Ca measures the viscous contribution to the surface deformation. The two numbers reflect the very different effects of the conservative and the non-conservative parts of the driving. In a system with static boundaries and vanishing *Reynolds number* we can express the velocity scale by the typical magnitude \bar{f}_{nc} of the non-conservative part of the driving force, namely $\bar{v} = \bar{x}^2 \bar{f}_{nc} / \eta$. This gives a definition of the capillary number similar to that of the Bond number,

$$Ca = \frac{\bar{f}_{nc} \bar{x}^2}{\gamma}. \quad (2.8)$$

In this sense, Ca provides also a measure for the spatial changes of the velocity field. For small Ca the flow is slow and changes smoothly, whereas for large Ca it may exhibit drastic gradients.

We propose our numerical scheme for the parameter regime where both, Ca , and Bo are of order 1 or less. Thus, pressure gradients and viscous forces can deform the free surface significantly. The surface tension is large enough, however, in order to keep the whole fluid domain together, and a pinch-off cannot occur. The viscosity renders the velocity field smooth over the whole fluid domain and prevents the existence of boundary layers. Because we consider only stationary flows in stationary domains according to equation (2.2) and (2.3) and because we have set the substrate's velocity to zero in equation (2.4), we will always obtain *pinned* contact-lines. A rolling or slipping droplet would raise additional challenges regarding the stress near the contact-line that are beyond the scope of this paper.

2.3. Preliminary work

A number of numerical algorithms tackling the problem of free surfaces have been proposed in the literature. They can be classified by either using a fixed grid and a function describing the position of the free surface, or moving the computational mesh together with the fluid domain. More information can be obtained from Behr & Abraham (2002), Popinet & Zaleski (1999) and Basaran & DePaoli (1994). Note that this reference list is far from being complete. Depending on the scales in the system and depending on the resulting deformation of the fluid domain different numerical approaches seem appropriate.

An established method of the first kind is the *continuum method* proposed by Brackbill

et al. (1992). They rephrased the boundary condition as a bulk force density, concentrated around the free surface. We have tested this method, which is implemented in the commercial fluid-dynamics program *FLUENT* using a *volume-of-fluid* discretisation. For a microfluidic system, in the parameter regime where the surface tension dominates, the method failed. In a simple testing example discretisation errors near the free surface contributed in the Navier–Stokes equations and were amplified in an uncontrolled manner. This gave rise to a spurious velocity field. Problems with this method have also been reported by Renardy & Renardy (2002).

Methods of the second kind, representing the free surface by a sharp interface are expected to work better in the microfluidic parameter regime. This class of algorithms is often referred to as the "moving mesh" or ALE methods. In their initial works Scriven and coworkers used spines to parameterise possible movements of the computational mesh (Saito & Scriven 1981; Kistler & Scriven 1983). They implemented a Newton method (by others also called *total linearisation method*) for a Galerkin/Finite element approximation scheme. Similar algorithms have been formulated in Cartesian coordinates using a height function (Cuvelier & Schulkes 1990, and references therein). We went back to the exciting works of Aris (1989) and Scriven (1960) where the fluidic flow inside a curved free surfaces is described. In the present paper we extend the Newton methods to arbitrary geometries, providing a completely covariant formulation of the free-surface boundary condition and its differential geometry.

An immediate result of our general description is an important improvement of the algorithm controlling possible mesh distortions at the free surface. Many algorithms implementing the weak form of the capillary boundary condition encounter intrinsic instabilities of the boundary mesh when significant changes of the free surface – moving or not – take place. For the program *surface evolver* (Brakke 1992) this manifests itself in shrinking and growing surface facets. Similar effects have been observed by Brinkmann (2002) and Bäsch (1998). Our formulation of the capillary free surface is such that it smoothly changes to the behaviour of a rubber band when the boundary mesh becomes distorted. This leads to an automatic regularisation of the mesh without explicit re-meshing or smoothing.

3. The physical origin of the free-surface boundary condition

In order to clarify the numerical treatment of the free-surface boundary condition we first explore the physical origins of the involved forces. We will then express each of them by the first variation of a functional.

The surface tension term $\gamma\kappa N_i$ arises from the fact that an extended interface between two different phases "costs" free energy (cf. Landau & Lifschitz 1966). To find the optimal configuration the surface is continually probing positions in its vicinity in order to minimise its free energy. When only a conservative force $f_i = -\Phi_{,i}$ is applied then the system is static ($v^i = 0$) and the free-surface boundary condition is equivalent to a minimisation of a free energy expression. This calculation is performed in appendix A.

Due to its thermodynamic origin, the surface tension term results from a first variation of a functional, also in the dynamic case with non-vanishing velocities. The contribution of the free surface A to the system's free energy is given by the integral of the surface tension γ over A , where dA denotes the infinitesimal surface area,

$$F = \int_A \gamma dA. \quad (3.1)$$

Any smooth surface in a D -dimensional space may be parameterised by $D-1$ surface

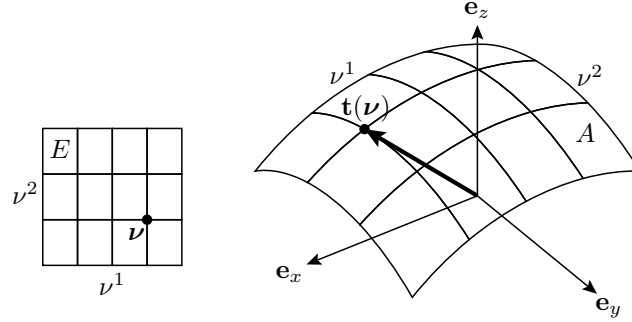


FIGURE 1. A sketch of the coordinate system on a 2D surface A . The surface coordinates ν are mapped from E onto A via the parameterisation vector $\mathbf{t}(\nu)$.

coordinates ν^α ($\alpha = 1, \dots, D-1$) which determine the coordinates $t^i(\nu^\alpha)$ of points in D -dimensional space on the surface. Both, surface and space coordinates are illustrated in figure 1. We note that in our numerical studies we restrict ourselves to $D = 2$. The general framework, however, remains valid for $D = 3$. The surface coordinates ν^α are taken from the parameter set $E \subset \mathbb{R}^{D-1}$. With ν running through E the whole free surface A is covered,

$$t^i: E \rightarrow \mathbb{R}: \nu \mapsto t^i(\nu) \quad (3.2)$$

$$A = \{\mathbf{e}_{(i)} t^i(\nu^\alpha) \mid \nu^\alpha \in E\}. \quad (3.3)$$

Here, $\mathbf{e}_{(i)}$ is the i th base vector in space. Throughout the paper we will always use Greek symbols for surface indices and Latin ones for space indices. The connection between surface and space coordinates is conveniently described by the surface derivatives of the parameterisation functions (cf. Aris 1989, p. 215),

$$t^i_{,\alpha}(\nu^\beta) = \frac{\partial t^i}{\partial \nu^\alpha}(\nu^\beta). \quad (3.4)$$

Understood as a contravariant D -dimensional space-vector, $t^i_{,\alpha}$ represent the components of the α th tangent vector \mathbf{T}_α to the surface. At the same time $t^i_{,\alpha}$ is a covariant surface-vector. We can now construct the components of the surface's metric tensor a_{ij} as the scalar products of these tangent vectors, namely

$$a_{\alpha\beta} = g_{ij} t^i_{,\alpha} t^j_{,\beta}, \quad a = \det(a_{\alpha\beta}). \quad (3.5)$$

The normal vector is then expressed as the normalised cross-product of two tangent vectors,

$$N_i = \frac{1}{2} \varepsilon_{ijk} \varepsilon^{\alpha\beta} t^j_{,\alpha} t^k_{,\beta}, \quad (3.6)$$

and the curvature κ is given as the trace of the tensor $b_{\alpha\beta}$, that is representing the second fundamental form of the surface,

$$\kappa = a^{\alpha\beta} b_{\alpha\beta} \quad \text{with} \quad (3.7)$$

$$b_{\alpha\beta} = t^i_{,\alpha\beta} N_i. \quad (3.8)$$

Using the parameterisation (3.2) of the free surface, we demonstrate in appendix B that the change of the free energy contribution F with respect to a variation of the surface vectors t^i is given by

$$\delta F[\delta \mathbf{t}] = \int_A \gamma t^j_{,\beta} g_{ij} a^{\alpha\beta} \delta t^i_{,\alpha} dA. \quad (3.9)$$

This expression coincides exactly with the surface tension term on the right-hand side of the free-surface boundary condition (2.5), i.e.,

$$\delta F[\delta \mathbf{t}] = - \int_A \gamma \kappa N_i \delta t^i dA - \int_A \gamma_{,\alpha} a^{\alpha\beta} t_{,\beta}^j g_{ij} \delta t^i dA, \quad (3.10)$$

see in appendix C. In this way, the curvature term κ containing second spatial derivatives is replaced by a product of two terms, each containing a first derivative. This method has been used in the literature in different contexts (Brakke 1992; Dziuk 1991; Bänsch 1998). Especially for numerical applications it is much more favourable to work only with first derivatives. Seen from a physical perspective, the version (3.9) of the equation is the more natural one. Here, one directly deduces that forces pulling along the tangent direction attempt to minimise the facet area of a mesh's boundary. This perspective will be used later for stabilising the computational mesh.

The left-hand side of (2.5), $\sigma_{ij} N^j$, is the normal fluidic stress at the boundary. We now will show how this term can be understood as the result of a variational principle. In a stationary system with rigid non-moving boundaries there is a balance between the power output due to *viscous dissipation* and the power input due to *external driving*. The total power output of the fluid, which we will denote with

$$P = \int_V \mathcal{P} dV = \int_V (\sigma^{ij} v_{i,j} - f^i v_i) dV, \quad (3.11)$$

vanishes. Additionally, for a prescribed domain V , the Stokes equations yield those velocity and pressure fields that render the local power extremal (Finlayson 1972, p. 271). Vice versa, from the vanishing first variation of P ,

$$\delta P[\delta p] = \int_V \frac{\partial \mathcal{P}}{\partial p} \delta p dV = - \int_V v_i^i \delta p dV \quad (3.12)$$

$$\begin{aligned} \delta P[\delta \mathbf{v}] &= \int_V \left(\frac{\partial \mathcal{P}}{\partial v_i} \delta v_i + \frac{\partial \mathcal{P}}{\partial v_{i,j}} \delta v_{i,j} \right) dV = \int_V (-f^i \delta v_i + \sigma^{ij} \delta v_{i,j}) dV \\ &= - \int_V (f^i + \sigma_{,j}^{ij}) \delta v_i dV + \oint_{\partial V} \sigma^{ij} N_j \delta v_i dA, \end{aligned} \quad (3.13)$$

the Stokes equations follow from setting the bulk contributions to zero. The boundary integral in (3.13) provides the fluidic stress in the free-surface boundary condition.

At this point we see that the two terms in the stress balance (2.5) have different physical origins. The surface tension is of thermodynamic (or rather of “thermostatic”) nature while the fluidic stress stems from dynamic considerations. Formally spoken, this difference is expressed by the different variations δv^i and δt^i in the expressions $\sigma_{ij} N^j \delta v^i$ in equation (3.13) and $\kappa \gamma N_i \delta t^i$ in equation (3.10). Already for dimensionality reasons they cannot be equal, neither can the functionals F and P be directly combined into one single variational principle.

From an algorithmic point of view we have to make a choice here: Either we approximate the free-surface boundary condition using the δv^i or the δt^i of the boundary positions as test-functions. In our Galerkin description of the problem we will use the ansatz functions, used for approximating their continuous counterparts, as test functions. Therefore, in order to acquire a consistent numerical algorithm we have to approximate both, velocity and the geometry parameterisation with Finite Elements of the very same order. It was stated by Bänsch (1998, p. 42, cf. also citations 49 and 50 therein) that in 3D a second-order approximation of the surface parameterisation yields a “good discrete curvature”, whereas a first-order one does not. At this point we are able to substantiate this numerical observation with the underlying physical mechanism. The argument is

similar to that for the celebrated Ladyzhenskaya–Babuska–Brezzi requirement that pressure and velocity gradients have to be approximated by the same order. From a physical perspective this is evident because both are components of the same stress tensor.

4. Two numerical systems

For free boundaries a twofold problem must be solved: (i) We have to find the unknown fluid domain V and (ii) we have to solve the Stokes equations (2.1) and (2.2) within V , using the boundary conditions (2.5) and (2.3). The latter themselves depend on the shape of V via the normal vector at the boundary. Both parts of the problem cannot be processed independently.

In principle, there exist two options to deal with this combined problem. One is to implement a single numerical system for both, the fluid variables p and v^i together with the geometry variables t^i . We will not follow this direction but rather consecutively solve two smaller systems, one for the fluid variables, depending on the current domain V , and a second one for the boundary shape of V . We have chosen this approach because the *fluidic system* can be kept linear, while the *geometry system* performs the highly nonlinear search for the correct boundary shape. Due to its nonlinearity, the geometry system has to be set up with an initial trial domain and updated stepwise until convergence is reached. After each step a new solution of the fluidic system is required.

The central question is, however, how the boundary condition should be assigned to these two systems in order to make them solvable and uniquely determined. It is clear that the no-slip boundary condition in (2.4) applies only to the fluidic system. The free-surface boundary condition needs further consideration at this point.

4.1. An ill-posed problem

By its very nature the tension force stays always normal on the surface of a fluid. Thus, only normal forces can be compensated by a free surface. As a simple example we consider a problem that is similar to the well-known catenary setup. A one-dimensional curve in 2D-space is fixed at its endpoints. A homogeneous force is assumed to act in the direction normal to the connecting line between the endpoints. If the curve is physically realised by a chain of rigid or elastic elements, its shape is given by a catenary or a parabola, respectively. But if the curve had to be realised by the free surface of a fluid, *this problem is ill-posed and does not possess a stationary solution*. The free surface then can only compensate normal forces and its shape results as a straight line. On the other hand, its curvature is zero and therefore cannot compensate the external force. Hence, no solution exists.

From this problem one may learn that the forces from the fluidic system, acting on a free surface, cannot be arbitrary but have to be compatible with the surface's shape. As a necessary condition the tangent projection of the normal stress has to vanish. Whenever tangential components emerge during the run of an algorithm, the result will be a numerical artefact. In the proposed scheme with two separated systems it is the fluidic system which must ensure the tangential component of the free boundary condition, i.e.,

$$(v_{i,j} + v_{j,i})N^i t_{,\alpha}^j = \gamma_{,\alpha} \quad \text{for all } \alpha. \quad (4.1)$$

For the velocity variables this is similar to a Neumann boundary condition. We thus expect the fluidic system to be fully determined by the boundary conditions (2.3), (2.4) and (4.1).

The geometry system is then responsible for the remaining normal component of the

stress balance (2.5),

$$-p + \eta(v_{i,j} + v_{j,i})N^i N^j = \gamma\kappa, \quad (4.2)$$

which is used as the update equation for the boundary. The free surface moves if equation (4.2) does not hold for a given trial boundary.

4.2. Second variations of the surface positions

In a first implementation we used a direct and explicit update algorithm moving the boundary into normal direction with a step-width that is determined by a weak form of equation (4.2), making use of the gradient descent (3.10), and a parameter τ controlling the step-width. Depending on the value of τ this method exhibited strong instabilities as demonstrated below in figure 2. Although advanced techniques for determining an apt value for τ seem to exist (cf. the program *surface evolver* by Brakke (1992)), we prefer a Newton–Raphson iterative method. This has the advantage of a faster convergence and a less strong dependence on τ . A minor disadvantage is that it requires an additional variation of the surface free energy for the assembly of the geometry system. Using the same calculus as in appendix B we find the second variation of the free energy contribution F of a one-dimensional free surface,

$$\begin{aligned} \delta^2 F[\delta \mathbf{t}, \delta \mathbf{t}] &= \delta \left(\int_A \gamma g_{ij} a^{\alpha\beta} t_{,\beta}^j \delta t_{,\alpha}^i dA \right) \\ &= \int_A \gamma \delta t_{,\alpha}^i g_{ij} a^{\alpha\beta} \delta t_{,\beta}^j dA - \int_A \gamma (\delta t_{,\alpha}^i g_{ik} a^{\alpha\psi} t_{,\psi}^k) (\delta t_{,\beta}^j g_{jl} a^{\beta\phi} t_{,\phi}^l) dA. \end{aligned} \quad (4.3)$$

In the 2D/3D case the corresponding variation contains two more terms that have been omitted here for brevity. The last integral turns out to cause instabilities in our implementation. The result becomes stable and still accurate if this term is omitted, as will be shown below.

It is not only the free energy contribution F that depends on the shape of the surface. Also, the flow velocity, and by this, the viscous stress and the pressure depend on the shape. The formulation of the Newton method requires also the change of the fluidic stress integral due to changes of the free boundary,

$$\delta \left(\int_A \sigma_{ij} N^j \delta t^i dA \right) = \int_A \delta t^i \sigma_{ij} \delta N^j dA + \int_E \delta t^i \sigma_{ij} N^j \delta \sqrt{a} d\boldsymbol{\nu} + \int_A \delta t^i \delta \sigma_{ij} N^j dA. \quad (4.4)$$

The first two integrals on the right-hand side contain the changes of the normal vector (3.6) and the infinitesimal surface area $dA = \sqrt{a} d\boldsymbol{\nu}$ due to changes of the boundary's shape. Both can be calculated along the lines of appendix B. The third integral expresses the change of the fluidic stress σ_{ij} at the boundary due to changes of its position. The shape changes are communicated to the flow and pressure fields via the boundary conditions (2.3) and (4.1) of the Stokes equations. Unfortunately, this very indirect response of the stress tensor on the changes of shape cannot be expressed exactly. We thus have to introduce an approximation into our approach by assuming that this term can be expressed by derivatives of the stress tensor, i.e.,

$$\delta \sigma_{ij} \approx \sigma_{ij,k} \delta t^k. \quad (4.5)$$

This means that the fluidic and the geometry system decouple to the extent that the stress tensor in the vicinity of the boundary is not affected by small boundary changes. Altogether, the right-hand side of equation (4.4) becomes approximately

$$\int_A \{ (\delta t^i \sigma_{ij} N^j) (\delta t^k g_{kl} a^{\alpha\beta} t_{,\beta}^l) - (\delta t^i \sigma_{ij} t_{,\alpha}^j) a^{\alpha\beta} (\delta t_{,\beta}^k N_k) + \delta t^i \sigma_{ij,k} N^j \delta t^k \} dA \quad (4.6)$$

which has been used for our implementation.

5. Discretisation details

We implemented the above equations by means of a Galerkin approximation scheme which is known to work well for minimisation problems. As variables we introduced the velocity components u and v in x - and y -direction, respectively, the pressure p , and additional variables r and s for the coordinates of the boundary parameterisation \mathbf{t} . The continuous fields are discretised using ansatz functions, weighted with the corresponding degrees-of-freedom (DoF),

$$u(\mathbf{x}) = \sum_d u_d \phi_d(\mathbf{x}), \quad v(\mathbf{x}) = \sum_d v_d \phi_d(\mathbf{x}), \quad (5.1)$$

$$p(\mathbf{x}) = \sum_d p_d \psi_d(\mathbf{x}), \quad (5.2)$$

$$r(\mathbf{x}) = \sum_d r_d \chi_d(\mathbf{x}), \quad s(\mathbf{x}) = \sum_d s_d \chi_d(\mathbf{x}), \quad (5.3)$$

where the sum runs over all DoFs. The fluid velocity components u, v are approximated by the second-order finite elements (FEs) ϕ and the pressure variable p by first-order FEs ψ . For the position variables r, s we have predominantly used second-order FEs, but for accuracy and other testing reasons we also tried first-order FEs. We denote the position FEs with χ . All FEs are of the Lagrange family (Deville *et al.* 2002), having ansatz functions that are 1 at exactly one node of the mesh and 0 at all others. The DoFs are then equal to the function values at the nodes. This property is most convenient for the coordinates of a node d that coincide with the position variables (r_d, s_d) .

5.1. The fluidic system

The fluidic system is implemented in a standard way. Equation (2.2) is tested with the second-order FEs ϕ , while the continuity equation (2.1) is tested with the first-order FEs ψ . Together, we have implemented the linear equation for the DoFs,

$$\begin{pmatrix} K_{uu} & 0 & K_{up} \\ 0 & K_{vv} & K_{vp} \\ K_{pu} & K_{pv} & 0 \end{pmatrix} \begin{pmatrix} \vec{u} \\ \vec{v} \\ \vec{p} \end{pmatrix} = \begin{pmatrix} L_u \\ L_v \\ 0 \end{pmatrix} \quad (5.4)$$

with the entry matrices K and entry vectors L given by

$$[K_{uu}]_{de} = \eta \int_V \nabla \phi_d \cdot \nabla \phi_e dV - \eta \oint_{\partial V} \phi_d \nabla \phi_e \cdot \mathbf{N} dA, \quad [K_{pu}]_{de} = - \int_V \psi_d \partial_x \phi_e dV, \quad (5.5)$$

$$[K_{vv}]_{de} = \eta \int_V \nabla \phi_d \cdot \nabla \phi_e dV - \eta \oint_{\partial V} \phi_d \nabla \phi_e \cdot \mathbf{N} dA, \quad [K_{pv}]_{de} = - \int_V \psi_d \partial_y \phi_e dV, \quad (5.6)$$

$$[K_{up}]_{de} = - \int_V (\partial_x \phi_d) \psi_e dV + \oint_{\partial V} \phi_d \psi_e N_x dA, \quad [L_u]_d = \int_V \phi_d f_x dV, \quad (5.7)$$

$$[K_{vp}]_{de} = - \int_V (\partial_y \phi_d) \psi_e dV + \oint_{\partial V} \phi_d \psi_e N_y dA, \quad [L_v]_d = \int_V \phi_d f_y dV. \quad (5.8)$$

All integrals are assembled in a loop over the elements and the sides of the mesh, using a fifth-order Gaussian quadrature rule. The fluidic system could likewise implement the stationary Navier–Stokes equations; we have chosen the Stokes equation for simplicity

reasons here. The boundary conditions are imposed using constraints for the matrix and the right-hand side in (5.4). Here, a constrained DoF u_d is expressed by an inhomogeneity plus a weighted sum of other DoFs,

$$u_d = w_d + \sum_{e \neq d} w_{de} u_e, \quad (5.9)$$

which represent the boundary condition in question. The DoF u_d is then completely eliminated from the linear system (5.4). By such constraint equations we implement weak formulations of the kinematic boundary condition (2.3)

$$0 = \sum_d \left(u_d \int_{\partial V} \phi_d N_x dA + v_d \int_{\partial V} \phi_d N_y dA \right), \quad (5.10)$$

the no-slip condition at the walls

$$0 = \sum_d \left(u_d \int_{\partial V} \phi_d T_x dA + v_d \int_{\partial V} \phi_d T_y dA \right), \quad (5.11)$$

and the tangent projection of the free-surface boundary condition (4.1) without the tension gradient term,

$$\begin{aligned} 0 = & \sum_d u_d \int_{\partial V} (2T_x N_x \partial_x \phi_d + (T_x N_y + T_y N_x) \partial_y \phi_d) dA \\ & + \sum_d v_d \int_{\partial V} (2T_y N_y \partial_y \phi_d + (T_x N_y + T_y N_x) \partial_x \phi_d) dA. \end{aligned} \quad (5.12)$$

They differ only in the values of w_{de} . The inhomogeneity w_d is zero in all three equations. Non-vanishing inhomogeneities result, if also the surface-gradient term are taken into account in (5.12), or if the rigid walls are moved in tangential direction in (5.11).

Equation (5.12) is equivalent to an ideal slip condition. It is known that an improper choice of the normal direction can cause spurious contributions to the velocity field (Behr 2004). In the absence of non-conservative forces we found no such spurious flow using our implementation. The fact that the formulation of the free boundary condition in terms of the DoF-constraints (5.12) cross-links all DoFs residing at boundary nodes, presents a serious problem. Each of the DoFs is in principle linked to all its neighbours on the boundary. This leads to a nearly filled system-matrix which is unfavourable regarding memory capacity and computing time. We found that an iterative method can overcome this problem. Instead of cross-linking a boundary DoF with all its neighbours, for some of them we take their old values, as is detailed in appendix D. After some iterations the full boundary condition (5.12) is established. The drawback of this scheme is that the constraint equations have to be re-assembled after every solution step of the fluidic system.

5.2. The geometry system

The geometry system employs a Newton method to perform the nonlinear search for the correct boundary position. This scheme corresponds to the search for the minimal free energy F , taking the fluidic stress into account. The boundary update equation can be written in a discretised form as

$$\begin{aligned} 0 = [L_r]_d(\vec{r}, \vec{s}, \vec{u}, \vec{v}, \vec{p}) & := \frac{\partial F}{\partial x_d} + \int_A \chi_d \sigma^{xj} N_j dA, \\ 0 = [L_s]_d(\vec{r}, \vec{s}, \vec{u}, \vec{v}, \vec{p}) & := \frac{\partial F}{\partial y_d} + \int_A \chi_d \sigma^{yj} N_j dA, \end{aligned} \quad (5.13)$$

where d runs over the DoFs for each geometry variable, and L and F are understood as functions of the arrays \vec{r} , \vec{s} , etc. containing the DoFs. For the Newton–Raphson method the geometry system repeatedly has to solve the linear system of equations (Bronshtein & Semendyayew 1985)

$$\begin{pmatrix} \partial[L_r]_d/\partial r_e & \partial[L_r]_d/\partial s_e \\ \partial[L_s]_d/\partial r_e & \partial[L_s]_d/\partial s_e \end{pmatrix}^{(\text{old})} \begin{pmatrix} \vec{r}_e^{(\text{new})} - \vec{r}_e^{(\text{old})} \\ \vec{s}_e^{(\text{new})} - \vec{s}_e^{(\text{old})} \end{pmatrix} = -\tau \begin{pmatrix} [L_r]_d \\ [L_s]_d \end{pmatrix}^{(\text{old})} \quad (5.14)$$

where $\tau \in [0, 1]$ is a step-size parameter. The advantage of the Newton algorithm is that this step-size needs no adjustment to the size of the FEs as it is the case for the direct explicit update. In all applications we have used values of τ between 0.1 and 1.0.

The search for the correct boundary shape is strongly nonlinear in the position variables. In order to remove the main nonlinearities, which are caused by the surface metric expressions \sqrt{a} and $a^{\alpha\beta}$, the nodes of the elements are moved to their corresponding coordinates (r_d, s_d) after each step of the geometry system. Then, all integrals can be performed directly on the elements' edges. Also the normal vector can be taken from the element's sides. In the previous section we used a convenient variational notation to express the change of the free energy contribution F by changes of the boundary parameterisation. Essentially the same equations are obtained by differentiating the discrete version of F with respect to the DoFs which are the nodal degrees of freedom of the corresponding variables. The only difference is that in the formulae the variation δt^i must be replaced by the vectorial test-function $\chi_d \mathbf{e}_i$, and the variation $\delta t_{,\alpha}^i$ by its tangent derivative $\mathbf{T}_\alpha \cdot \nabla \chi_d \mathbf{e}_i$.

5.3. Controlling the tangential displacements of boundary nodes

For a given discretisation we must not only find the correct boundary shape, but its discretisation should also remain well-proportioned. Very long and very short element sides cause badly conditioned matrices and make the whole algorithm unstable. Several algorithms implementing the weak form of the free-surface boundary condition encounter these intrinsic instabilities of the boundary mesh. For the program *surface evolver* this manifests itself in shrinking and growing surface facets. It is therefore recommended to monitor the mesh quality and remove too small or split too large elements (Brakke 1992). Similar effects have been observed by Brinkmann (2002).

In view of the previously introduced *ill-posed problem*, we propose a solution for this complication. The presence of incompatible forces may easily destroy a free surface which essentially attempts to minimise the lengths $A_{(m)}$ of the free-surface sides in each element m . If the boundary were not a free surface but a rubber band, minimising the squared length $A_{(m)}^2/2$, it would be able to compensate an arbitrary force.

Because all fluidic stresses are constrained to have only normal components, we are free to use additional tangential force components for keeping the boundary mesh as regular as possible. We do this during assembly of the system matrices by weighting the surface tension by the element's side length $A_{(m)}$, divided by the average length $\langle A_{(m)} \rangle$ of all element sides contributing to the free surface. Of course, this weighting factor becomes ineffective if all sides have equal length. Any length difference of adjacent sides causes an additional force that tries to equalise them. The tension forces for each element side are then equivalent to a first variation of the functional $\gamma A_{(m)}^2/(2\langle A_{(m)} \rangle)$, which describes a rubber band with Hookean forces,

$$\frac{\gamma}{2\langle A_{(m)} \rangle} \delta(A_{(m)}^2)[\delta \mathbf{t}] = \gamma \frac{A_{(m)}}{\langle A_{(m)} \rangle} \delta A_{(m)}[\delta \mathbf{t}]. \quad (5.15)$$

The second variations of $A_{(m)}$ and $A_{(m)}^2/2$ are not proportional to each other,

$$\frac{\gamma}{2\langle A_{(m)} \rangle} \delta^2(A_{(m)}^2)[\delta\mathbf{t}, \delta\mathbf{t}] = \gamma \frac{A_{(m)}}{\langle A_{(m)} \rangle} \delta^2 A_{(m)}[\delta\mathbf{t}, \delta\mathbf{t}] + \gamma \frac{1}{\langle A_{(m)} \rangle} (\delta A_{(m)}[\delta\mathbf{t}])^2 \quad (5.16)$$

In the implementation we took only the first term on the right-hand side. In this sense we did not strictly implement the behaviour of a rubber band, but yet a stabilised version of the free-surface tension terms. For a regularly spaced boundary mesh the factors do not change the behaviour of the free surface. After convergence all boundary sides of the mesh representing the free surface have equal lengths.

5.4. Summary of the algorithm

Here, we provide a short overview of the algorithm that we have implemented. The steps are as follows:

- (1) Choose an initial mesh and initial ambient pressure p_0
- (2) Until convergence repeat the following steps:
 - (a) Smooth the inner mesh if it is too distorted,
 - (b) Solve the fluidic system for p , u and v ,
 - (c) Calculate p_1 by subtracting the average from p ,
 - (d) Solve the geometry system for the new boundary by searching for the value of p_0 that keeps the volume unchanged,
 - (e) Set the mesh boundary nodes to the values of the geometry system.

The fluidic system is assembled according to equations (5.4)–(5.8) with constraints that account for the proper boundary conditions. To give the full algorithm at this point, we summarise also the terms of the geometry system. The update equation (5.14) is written as

$$\begin{pmatrix} K_{rr} & K_{rs} \\ K_{sr} & K_{ss} \end{pmatrix} \begin{pmatrix} \vec{r}^{(\text{new})} \\ \vec{s}^{(\text{new})} \end{pmatrix} = -\tau \begin{pmatrix} L_r \\ L_s \end{pmatrix} + \begin{pmatrix} K_{rr} & K_{rs} \\ K_{sr} & K_{ss} \end{pmatrix} \begin{pmatrix} \vec{r}^{(\text{old})} \\ \vec{s}^{(\text{old})} \end{pmatrix} \quad (5.17)$$

with entries that are assembled per element m ,

$$\begin{aligned} [L_r^{(m)}]_d &= \int_{A_{(m)}} \chi_d (\mathbf{e}_x \cdot \boldsymbol{\sigma} \cdot \mathbf{N}) dA + \frac{\gamma A_{(m)}}{\langle A_{(m)} \rangle} \int_{A_{(m)}} (\boldsymbol{\nabla} \chi_d \cdot \mathbf{T})(\mathbf{e}_x \cdot \mathbf{T}) dA \\ [K_{rr}^{(m)}]_{de} &= - \int_{A_{(m)}} \chi_d \chi_e (\mathbf{e}_x \cdot \boldsymbol{\nabla} p)(\mathbf{e}_x \cdot \mathbf{N}) dA \\ &\quad + \int_{A_{(m)}} \chi_d (\boldsymbol{\nabla} \chi_e \cdot \mathbf{T}) \{(\mathbf{e}_x \cdot \boldsymbol{\sigma} \cdot \mathbf{N})(\mathbf{e}_x \cdot \mathbf{T}) - (\mathbf{e}_x \cdot \boldsymbol{\sigma} \cdot \mathbf{T})(\mathbf{e}_x \cdot \mathbf{N})\} dA \\ &\quad + \frac{\gamma A_{(m)}}{\langle A_{(m)} \rangle} \int_{A_{(m)}} (\boldsymbol{\nabla} \chi_d \cdot \mathbf{T})(\boldsymbol{\nabla} \chi_e \cdot \mathbf{T}) dA \end{aligned} \quad (5.19)$$

$$\begin{aligned} [K_{rs}^{(m)}]_{de} &= - \int_{A_{(m)}} \chi_d \chi_e (\mathbf{e}_x \cdot \boldsymbol{\nabla} p)(\mathbf{e}_y \cdot \mathbf{N}) dA \\ &\quad + \int_{A_{(m)}} \chi_d (\boldsymbol{\nabla} \chi_e \cdot \mathbf{T}) \{(\mathbf{e}_x \cdot \boldsymbol{\sigma} \cdot \mathbf{N})(\mathbf{e}_y \cdot \mathbf{T}) - (\mathbf{e}_x \cdot \boldsymbol{\sigma} \cdot \mathbf{T})(\mathbf{e}_y \cdot \mathbf{N})\} dA. \end{aligned} \quad (5.20)$$

The remaining entries can be obtained by permutation of x and y and of r and s , respectively. Again, constraints have been used to keep the contact-lines pinned.

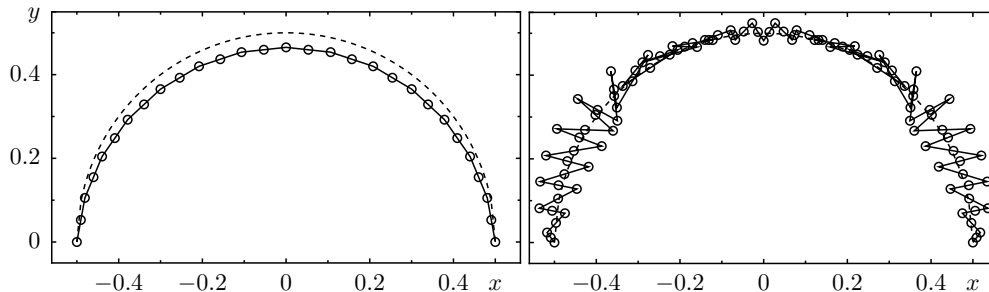


FIGURE 2. The stability of a direct explicit update algorithm strongly depends on the ratio of the step-size τ and the element size. We have used the same $\tau = 0.05$ for two different numbers of approximating FEs (first-order). The left panel depicts the converged result for 14 FEs after more than 500 steps. The right panel shows a mesh with 52 FEs after only 12 steps. For this combination of step-size and element size the direct update algorithm is unstable, and the mesh was completely destroyed a few steps later. Using second-order FEs the instability was similar. The dashed half-circle indicates both the initial geometry and the exact solution.

6. Numerical experiments

We performed all our test cases for a 2-dimensional fluid. The programs were written using the open-source C++ library *libmesh* (Kirk *et al.* 2004) which allows to change the elements' geometry in a user's routine and provides a powerful constraint method. We assumed a constant surface tension over the whole free surface, omitting the gradient term in the boundary condition (2.5).

6.1. The instability of the direct explicit update algorithm

Our first numerical example shows how the stability of the direct and explicit update algorithm depends on the step-size parameter τ . The allowed range of τ strongly depends on the size of the elements, the curvature, etc. Figure 2 depicts two examples for a simple half-circular geometry, where the direct update is stable for 14 FEs and a given step-size while it is unstable for 52 FEs and the same step-size.

6.2. Testing the accuracy of the Newton algorithm

In order to check the accuracy of the proposed algorithm we have tested two cases that can be solved exactly. Similar to the calculation in appendix A a prescribed pressure determines the free surface's shape. Then, the approximation in equation (4.5) becomes exact and simplifies to

$$\delta\sigma_{ij} = -g_{ij}p_k\delta t^k. \quad (6.1)$$

Thus, all approximation errors are due to the discretisation of the surface tension.

In the most simple situation a homogeneous pressure field deforms the boundary into a circular arc with radius $R = -1/\kappa = p/\gamma$. Figure 3 shows a free surface shape approximated by the sides of 14 second-order FEs. In dimensionless units the surface tension is 1, and the prescribed pressure $p = 2$ produces a circle with radius $R = 1/2$ as the exact solution. The relative error of the numerically resulting radius, and thus also of the curvature, is about 1.2×10^{-5} . Here, it is crucial that the geometry variables are approximated to second order. The same algorithm with a first-order approximation gives a relative error of 5.0×10^{-3} . The resulting boundary shape can be seen in the left panel of figure 2.

In our third example the pressure varies along the surface. Regarding the discretisation errors of the tension this is already the general case, because our algorithm allows stress

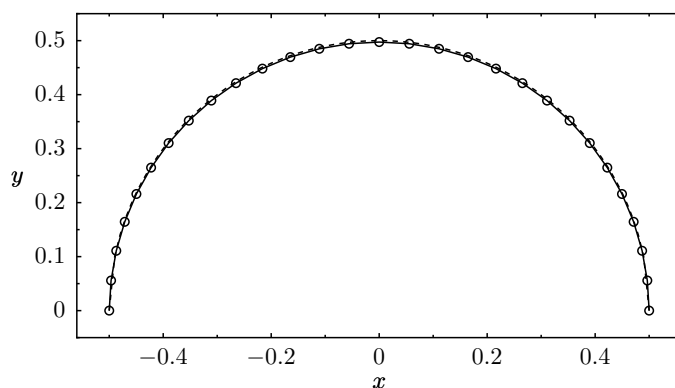


FIGURE 3. A prescribed homogeneous pressure $p = 2$ bends the free surface into a half-circle with radius $1/2$ (with $\gamma = 1$). The approximation with only 14 second-order FEs is excellent, showing a relative error of only 1.2×10^{-5} . Both endpoints of the boundary are fixed. The dashed half-circle indicates both the exact solution and the initial shape.

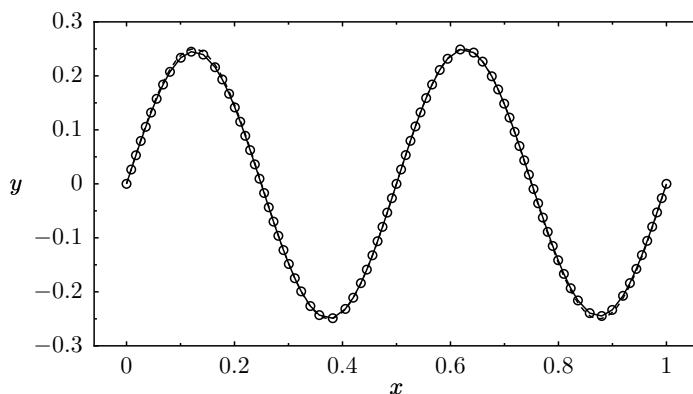


FIGURE 4. The prescribed pressure of equation (6.2) bends the free boundary into the expected sinusoidal boundary shape $y = h(x) = 0.25 \sin(4\pi x)$ which is indicated by the dashed curve. The initial geometry was the straight connection between the fixed endpoints. The approximation with 41 second-order FEs recovers the expected curvature up to a small relative error of 5.4×10^{-4} at the maxima. The boundary nodes are indicated by circles. The elements' side-lengths vary only by $\pm 0.25\%$. This small deviation demonstrates that the mesh regularisation method does not influence the final behaviour of the free boundary. The relative approximation error decreases when more FEs are used: For 181 elements it is 1.2×10^{-5} (not shown). The approximation quality is dramatically worse for 41 first-order FEs, yielding an estimated error of 2.0×10^{-1} (not shown).

only in normal direction of the boundary. It makes no difference whether the stress is due to pressure or viscosity. As in the previous example we apply a prescribed pressure for which the resulting boundary shape is known. Figure 4 shows the approximation of a sinusoidal boundary height function $y = h(x) = \alpha \sin(\beta x)$ that is caused by the corresponding pressure field

$$p(x, y) = -\frac{\kappa(x)}{\gamma} = -\frac{1}{\gamma} \frac{h''(x)}{[1 + h'^2(x)]^{3/2}} = \frac{1}{\gamma} \frac{\alpha \beta^2 \sin(\beta x)}{[1 + \alpha^2 \beta^2 \cos^2(\beta x)]^{3/2}}. \quad (6.2)$$

Here, we expect the same discretisation errors as in the previous example. The curvature's relative error is larger but still small enough to return the expected boundary shape within reasonable accuracy. The relative error decreases with the number of ap-

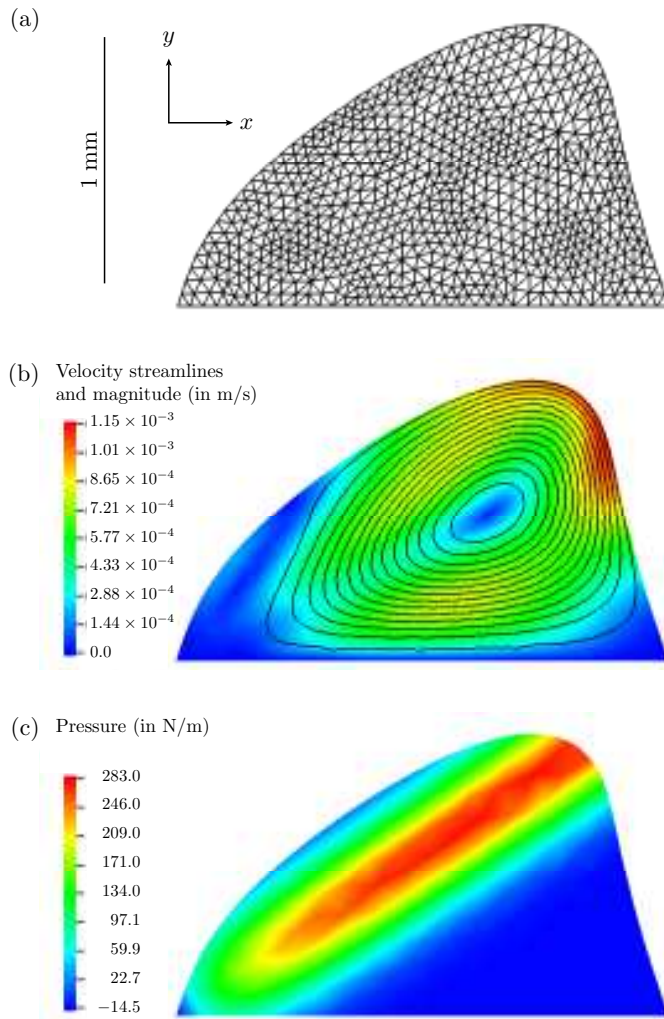


FIGURE 5. A deformed micro-droplet, sitting on a flat substrate. The contact area with the substrate is fixed, and the droplet’s shape is deformed by the internal pressure and viscous flow. The material properties are chosen to fit those of an experimentally observed droplet in figure 4 of the publication by Wixforth *et al.* (2004), where a similar deformation can be seen. The fluid is water, surrounded by air at room temperature. Its two-dimensional “volume” is that of a half-circle with radius 1 mm. Panel (a) illustrates the computational grid, consisting of second-order elements (all nodes are shown). Panels (b) and (c) depict the flow and the pressure, respectively. Note that the deformation is predominantly caused by the pressure which directly corresponds to the conservative part of the driving force density shown in figure 6. The chosen initial shape in the calculation was a half-circle with the same volume.

proximating elements and is much larger, maybe intolerably large, when a first-order approximation is used.

6.3. A deformed micro-droplet

Finally, we present an example that cannot be solved analytically. It is motivated by the experimental observation of an internally streaming micro-droplet shown in figure 4 of the publication by Wixforth *et al.* (2004). The resulting droplet shape, the velocity profile and the pressure field can be seen in figure 5. The initial shape was a half-circle with

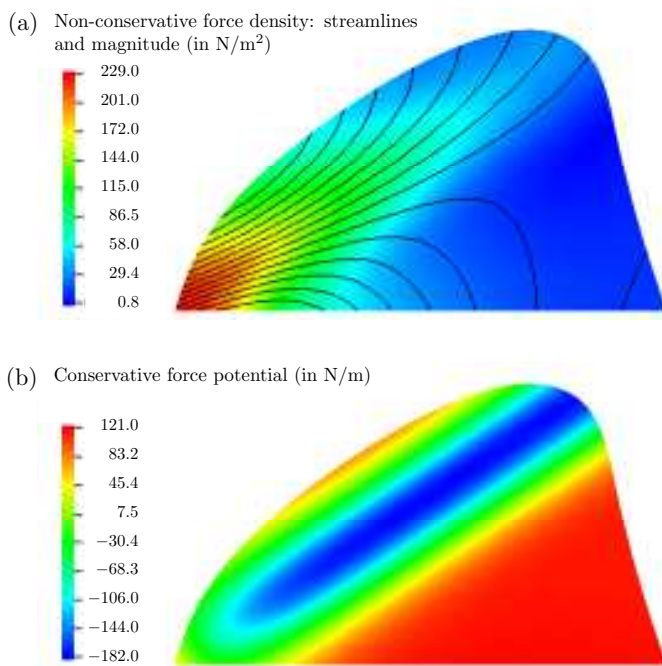


FIGURE 6. The force density that causes the streaming in the droplet in figure 5. Panel (a) depicts the non-conservative part that causes the flow, (b) shows the potential of the conservative part that contributes only to the pressure. The same non-conservative force density has also been used in figure 7.

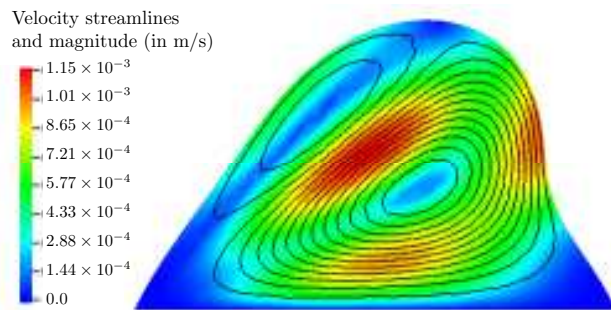


FIGURE 7. A similar micro-droplet as in figure 5, deformed only by viscous stress at the boundary. The flow is driven by the non-conservative force density depicted in figure 6a. The conservative part has been chosen such that the pressure is constant inside the droplet. In order to obtain a comparable deformation we have used a 10^5 times smaller surface tension than that of a water-air interface.

radius 1 mm. The deformed boundary contains not only the initial negative curvature (of the half-circle) but also a region with positive curvature at the right flank of the droplet.

In the experiment the internal flow is agitated by a surface-acoustic wave (SAW) due to the *acoustic streaming effect* hitting the droplet from the left. Because the very details of the SAW's impact are not known, we here model it by a bulk force depicted in figure 6. The force is concentrated in a narrow channel starting at the left contact point where the SAW hits the fluid and continuing into the fluid under an angle of approximately 35 degrees from the x -axis. The non-conservative part of the force should reproduce the

experimentally observed typical flow velocities about 1 mm/s. Using the surface tension of a water–air interface with $\gamma = 72.8 \times 10^{-3}$ N/m and the viscosity of water, we observed that the viscous stress of the velocity field is not strong enough to deform the free surface. In order to achieve a deformation as strong as in the experiment we additionally need a strong conservative force resulting in a pressure field. In this example the shape deformation is mainly caused by the pressure. This corresponds to the parameter regime $Ca \ll Bo$.

In a further example we show that our algorithm can likewise produce stable results in the parameter regime $Bo \ll Ca$. In figure 7 we show a droplet that is deformed only by viscous stress at the boundary. We have used the same non-conservative force as in the previous example but changed the conservative part such that it always diminishes the pressure. Using the same water–air interface as in the previous example the droplet would hardly be deformed. To obtain a comparable deformation as in the previous case we took a 10^5 times smaller artificial surface tension.

7. Summary and Outlook

Within this work we have presented a weak formulation of free-surface boundary problems in arbitrary coordinate systems. The steps of the derivation are physically and mathematically founded using variational techniques for the Stokes equations and the differential geometry of the surface. The resulting method is not restricted to the Stokes equations, but also valid for Navier–Stokes.

As a main result we find that the geometry variables for the parameterisation of the free surface should be approximated on the same level of accuracy as the velocity variables. This substantiates numerical observations reported by Bänsch (1998).

The fully covariant derivation opens the possibility to utilise the powerful differential geometric description of the surface for the Finite-Element implementation of the Navier–Stokes equations. This technique also provides a natural approach to treat surfaces and interfaces with a richer behaviour such as lipid vesicles containing bending stiffness, area constraints and much more. Many potential applications can be found in the literature on lipid vesicle geometry, where more complicated expressions for the surface’s free energy contribution are in use (Güven 2004; Capovilla *et al.* 2003; Seifert 1997).

Another decisive benefit of our method is the control of mesh distortions at a free surface. Many algorithms implementing the weak form of the capillary free boundary condition encounter intrinsic instabilities of the boundary mesh. Our formulation includes a smooth transition to the behaviour of a rubber band when the boundary mesh becomes distorted. This leads to an inherent regularisation of the mesh without affecting the behaviour of the free surface.

The qualities of our numerical approach are exemplified for an experimentally observed micro-droplet sitting on a flat substrate (see Wixforth *et al.* 2004, figure 4) that is agitated by a surface-acoustic wave. The accuracy of the numerically obtained free surface shape, that was tested in two further examples, allows a qualitative characterisation of the driving force density. It turned out that a strong conservative force component must have caused the observed deformation.

We gratefully acknowledge our experimental partners in the group of Prof. Achim Wixforth, Univ. Augsburg and the developers of the *libmesh* project for providing us with a Finite Element library. This work was supported by the *Deutsche Forschungsgemeinschaft* (DFG) via grant 1517/25-1, SFB 486 and the *Graduiertenkolleg: Nichtlineare Probleme in Analysis, Geometrie und Physik*.

Appendix A. A static droplet in Cartesian coordinates

The aim of this appendix is to recall the variational techniques in a simple 3D Cartesian setup before going to arbitrary coordinates in appendix B. The argumentation is similar to that by Cuvelier & Schulkes (1990).

We describe the special case where the fluid's free surface A in 3D can be described by a height function

$$A: z = h(x, y) \quad (\text{A } 1)$$

which is non-zero over a certain region $(x, y) \in E$. The Stokes equations for the static situation with a conservative force $f_i = -\Phi_{,i}$ reduce to

$$0 = -p_{,i} - \Phi_{,i} \quad (\text{A } 2)$$

with the solution $p(\mathbf{x}) = p_0 - \Phi(\mathbf{x})$. The undetermined homogeneous term p_0 will later be identified as the Lagrange multiplier for the constraint of constant volume $V = \int_E dx dy h(x, y)$.

The free energy of the system consists of the surface-integral over the constant surface tension and the volume-integral over the potential

$$F = \gamma \int_A dA + \int_V \Phi dV = \int_E \mathcal{F}(x, y) dx dy \quad \text{with} \quad (\text{A } 3)$$

$$\mathcal{F}(x, y) = \gamma \sqrt{1 + (\partial_x h(x, y))^2 + (\partial_y h(x, y))^2} + \int_0^{h(x, y)} \Phi(x, y, z) dz. \quad (\text{A } 4)$$

The Euler-Lagrange equation for finding the extremal F by varying h is then

$$0 = \frac{\partial \mathcal{F}}{\partial h} - \frac{\partial}{\partial x} \frac{\partial \mathcal{F}}{\partial (\partial_x h)} - \frac{\partial}{\partial y} \frac{\partial \mathcal{F}}{\partial (\partial_y h)} \quad (\text{A } 5)$$

$$= \Phi(x, y, h(x, y)) - \gamma \kappa(x, y) \quad (\text{A } 6)$$

where κ is the curvature of A , given by (cf. Aris 1989, p. 217)

$$\kappa(x, y) = \frac{(\partial_x^2 h)(1 + (\partial_y h)^2) + (\partial_y^2 h)(1 + (\partial_x h)^2) - 2(\partial_x h)(\partial_y h)(\partial_x \partial_y h)}{[1 + (\partial_x h)^2 + (\partial_y h)^2]^{3/2}} \quad (\text{A } 7)$$

$$= \frac{\partial}{\partial x} \frac{\partial_x h(x, y)}{[1 + (\partial_x h)^2 + (\partial_y h)^2]^{1/2}} + \frac{\partial}{\partial y} \frac{\partial_y h(x, y)}{[1 + (\partial_x h)^2 + (\partial_y h)^2]^{1/2}}. \quad (\text{A } 8)$$

Because the pressure is given by the potential, the Euler-Lagrange equation is equivalent to the free-surface boundary condition for a static fluid,

$$-p(x, y, h(x, y)) + p_0 = \gamma \kappa(x, y). \quad (\text{A } 9)$$

At this point it is easy to see that p_0 plays the role of a Lagrange multiplier for a volume constraint. Adding the term

$$\lambda V = \lambda \int_E dx dy h(x, y) \quad (\text{A } 10)$$

to F gives an additional constant λ in the Euler-Lagrange equation, just as the pressure offset p_0 . Because p_0 is undetermined we may identify them.

Appendix B. Variational calculus for the surface's parameterisation

In order to prove equality (3.9) we express the change of the surface's free energy functional (3.1) by the change of the Jacobi determinant \sqrt{a} of the surface parameterisation.

With the infinitesimal surface area $dA = \sqrt{a} d\nu$ the variation of the surface free energy becomes

$$\delta F[\delta \mathbf{t}] = \delta \left(\int_A \gamma dA \right) = \int_E \gamma \delta \sqrt{a} d\nu = \int_E \gamma \frac{\partial \sqrt{a}}{\partial t^i_{,\alpha}} \delta t^i_{,\alpha} d\nu. \quad (\text{B } 1)$$

The dependence of \sqrt{a} on the tangent vectors follows from its definition as the determinant of the surface metric. In the 2D/3D case it reads

$$a = \begin{vmatrix} a_{11} & a_{12} \\ a_{21} & a_{22} \end{vmatrix} = \frac{1}{2} \epsilon^{\alpha\gamma} \epsilon^{\beta\delta} a_{\alpha\beta} a_{\gamma\delta} = \frac{1}{2} \epsilon^{\alpha\gamma} \epsilon^{\beta\delta} g_{ij} g_{kl} t^i_{,\alpha} t^j_{,\beta} t^k_{,\gamma} t^l_{,\delta} \quad (\text{B } 2)$$

where $\epsilon^{\alpha\beta}$ is the permutation symbol in 2D,

$$\epsilon^{\alpha\beta} = \begin{cases} 0 & \alpha = \beta \\ +1 & \alpha = 1, \quad \beta = 2 \\ -1 & \alpha = 2, \quad \beta = 1 \end{cases} \quad (\text{B } 3)$$

which is a relative surface tensor with weight +1. The absolute tensor results as

$$\varepsilon^{\alpha\beta} = \frac{\epsilon^{\alpha\beta}}{\sqrt{a}}. \quad (\text{B } 4)$$

This is analogous to the 3D antisymmetric tensor, described in detail by Aris (1989, p. 145). With the antisymmetric tensor we obtain the inverse surface metric as

$$a^{\alpha\beta} = \varepsilon^{\alpha\gamma} \varepsilon^{\beta\delta} a_{\gamma\delta}. \quad (\text{B } 5)$$

A formal derivative of (B 2) now yields

$$\frac{\partial a}{\partial t^i_{,\alpha}} = 2g_{ij} t^j_{,\beta} \varepsilon^{\alpha\gamma} \varepsilon^{\beta\delta} a_{\gamma\delta} = 2a g_{ij} a^{\alpha\beta} t^j_{,\beta} \quad \text{and} \quad (\text{B } 6)$$

$$\frac{\partial \sqrt{a}}{\partial t^i_{,\alpha}} = \frac{1}{2\sqrt{a}} \frac{\partial a}{\partial t^i_{,\alpha}} = \sqrt{a} g_{ij} a^{\alpha\beta} t^j_{,\beta} \quad (\text{B } 7)$$

which can be inserted into (B 1) to give the desired result (3.9).

For a 1D curve in 2D space the same formula can be derived, but the notation is a little confusing. Summation over the single surface index makes no sense, nevertheless, we still have to distinguish between co- and contravariant relative tensors.

$$a = a_{11} = g_{ij} t^i_{,1} t^j_{,1} \quad (\text{B } 8)$$

$$a^{11} = 1/a_{11} \quad \text{because} \quad a^{11} a_{11} = a^{\alpha\beta} a_{\alpha\beta} = 1. \quad (\text{B } 9)$$

The formal derivative then becomes

$$\frac{\partial \sqrt{a}}{\partial t^i_{,1}} = \frac{1}{2\sqrt{a}} 2g_{ij} t^j_{,1} = \sqrt{a} g_{ij} t^j_{,1} \frac{1}{a_{11}} = \sqrt{a} g_{ij} t^j_{,1} a^{11} \quad (\text{B } 10)$$

which completes the result for the 1D/2D case.

Appendix C. Partial integration of the curvature

In order to see that equation (3.10) follows from equation (3.9) we remove the surface covariant derivative from $\delta t^i_{,\alpha}$ by a partial integration and obtain

$$\delta F[\delta \mathbf{t}] = - \int_A \gamma a^{\alpha\beta} t^i_{,\alpha\beta} g_{ij} \delta t^j - \int_A \gamma_{,\beta} a^{\alpha\beta} t^i_{,\alpha} g_{ij} \delta t^j + \oint_{\partial A} \gamma \nu_{\beta} a^{\alpha\beta} t^i_{,\alpha} g_{ij} \delta t^j \quad (\text{C } 1)$$

where the covariant surface vector ν_β is tangent to A and normal to ∂A . We can express the surface derivatives $t^i_{,\alpha\beta}$ by the tensor $b_{\alpha\beta}$ of the second fundamental form of the surface from equation (3.8) (cf. Aris 1989, p. 216),

$$t^i_{,\alpha\beta} = b_{\alpha\beta} N^i, \quad (\text{C } 2)$$

arriving at

$$a^{\alpha\beta} t^i_{,\alpha\beta} = a^{\alpha\beta} b_{\alpha\beta} N^i = \kappa N^i. \quad (\text{C } 3)$$

We have used the definition of the curvature as the trace of the tensor of the second fundamental form as in equation (3.7). For the 2D/3D case this is twice the mean curvature $\kappa = 2H = a^{\alpha\beta} b_{\alpha\beta}$, for the 1D/2D case we have only one entry $\kappa = a^{11} b_{11}$.

As consistent with the standard literature (Landau & Lifschitz 1966; Aris 1989), δF from equation (3.9) consists of a curvature term in normal direction

$$-\gamma \kappa N^i \quad (\text{C } 4)$$

and a term accounting for the surface-gradient of γ . The space vector

$$-t^i_{,\alpha} a^{\alpha\beta} \gamma_{,\beta} =: -T^i_\alpha \nabla_\alpha \gamma \quad (\text{C } 5)$$

is tangent to the surface. The third term on the right-hand side of equation (C 1), which is an integral over the contact-line ∂A , vanishes because for a pinned droplet $\delta t^i = 0$ vanishes on the contact-line.

Appendix D. Invoking constraints for the slip boundary condition

The tangential components of the free-surface boundary condition correspond to a slip boundary condition. When this condition is expressed as a set of constraints for the DoFs, we obtain one equation like (5.12) per each DoF at the free surface. Because the derivatives of the ansatz functions ϕ from (5.1) generally do not vanish at proximate nodes, the constraint equations contain non-vanishing weights for all DoFs that are located on the same element. Therefore, the constraints for DoFs that are connected to two adjacent elements create inter-dependencies of DoFs also on other elements. This is illustrated in figure 8a. As a result, all DoFs on the free surface implicitly depend on each other. After the constraints are re-sorted such that DoFs are constrained only in terms of non-constrained ones, it turns out that the free-surface DoFs depend on all DoFs in the element layer near the surface.

As a strategy to avoid this full dependency we replace the constraint equation of type (5.9) by

$$u_d = w_d + \sum_{e \in \Lambda_d} w_{de} u_e + \sum_{e \in \bar{\Lambda}_d} w_{de} u_e^{(\text{old})}, \quad (\text{D } 1)$$

where the sums run over two complementary sets Λ_d and $\bar{\Lambda}_d$. The DoFs in Λ_d contribute to the constraint for u_d in the usual way, while those in $\bar{\Lambda}_d$ have been substituted by their old values $u_e^{(\text{old})}$ and thus contribute to the inhomogeneity. There is some freedom in the choice, which of the participating DoFs in one element are in Λ_d and which are taken into $\bar{\Lambda}_d$. We found that the combination illustrated in figure 8b works well: For the DoFs located at element vertices the DoFs belong to adjacent nodes on the free surface are taken as inhomogeneities; all other constraining DoFs are located at inner nodes and are not constrained. The DoFs located at the second-order nodes on the free surface acquire their full constraints. When all constrained DoFs are expressed by non-constrained DoFs, then the resulting constraint equations will only contain DoFs that are located at inner

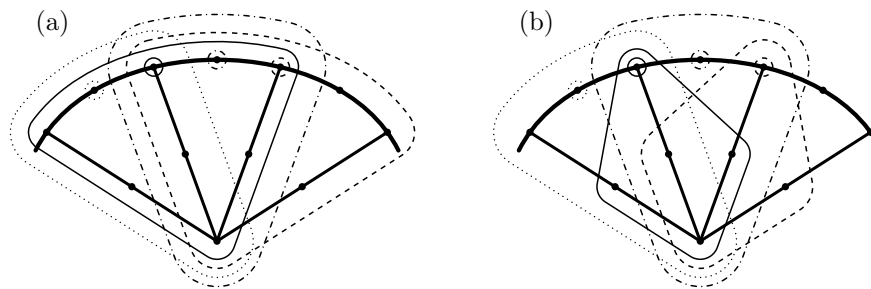


FIGURE 8. A sketch of the cross-dependencies among the DoFs located on three elements. The free surface is indicated by the thick curve. Constrained DoFs are surrounded by small circles. The nodes carrying the corresponding constraining DoFs are surrounded by curves drawn in the same style (solid and dashed for vertices; dotted and dash-dotted for second-order nodes). Panel (a) depicts the full inter-dependencies while in (b) the DoFs located at vertices depend only on DoFs located at inner nodes. By taking the values of the missing adjacent DoFs located on the free surface as inhomogeneities instead of constraints in (b) constraints are decoupled. The correct constraint equations are then established after some iteration steps.

nodes of three adjacent elements. This presents a sufficient decoupling of the constraint equations to yield an efficient algorithm.

Although the boundary condition given by (D 1) is not the correct one when the correct velocity field has not yet been found, it still improves as the velocity field ameliorates. Thus, there is hope that the correct boundary condition is established by the successive use of (D 1) using better and better values for the values $u_e^{(\text{old})}$. In numerical experiments the scheme for splitting the cross-dependencies as illustrated in figure 8b turned out to be the only one that works. In the examples of figures 5 and 7 it took about 20 iteration steps to establish the correct boundary condition. This could be easily observed because after the first iteration step the velocity field exhibited oscillations at the boundary nodes that ceased during iteration.

REFERENCES

- ARIS, R. 1989 *Vectors, Tensors, and the Basic Equations of Fluid Mechanics*. New York: Dover Publications.
- BÄNSCH, E. 1998 *Numerical methods for the instationary Navier-Stokes equations with a free capillary surface*. Freiburg: Albert-Ludwigs-Universität Freiburg, habilitation thesis.
- BASARAN, O. A. & DEPAOLI, D. W. 1994 Nonlinear oscillations of pendant drops. *Phys. Fluids* **6**, 2923.
- BEHR, M. 2004 On the application of slip boundary condition on curved boundaries. *Int. J. Numer. Meth. Fluids* **45**, 43.
- BEHR, M. & ABRAHAM, F. 2002 Free-surface flow simulations in the presence of inclined walls. *Comput. Methods Appl. Mech. Engrg.* **191**, 5467.
- BRACKBILL, J. U., KOTHE, D. B. & ZEMACH, C. 1992 A continuum method for modeling surface tension. *J. Comput. Physics* **100**, 335.
- BRÄKKE, K. A. 1992 The surface evolver. *Experimental Mathematics* **1**, 141.
- BRINKMANN, M. 2002 Benetzung lateraler strukturierter Oberflächen. PhD thesis, Universität Potsdam, Potsdam.
- BRONSHTEIN, I. N. & SEMENDYAYEW, K. A. 1985 *Handbook of Mathematics*. Thun, Frankfurt a. M.: Harri Deutsch.
- CAPOVILLA, R., GUVEN, J. & SANTIAGO, J. A. 2003 Deformations of the geometry of lipid vesicles. *J. Phys. A: Math. Gen.* **36**, 6281.
- CUVELIER, C. & SCHULKES, R. M. S. 1990 Some numerical methods for the computation of capillary free boundaries governed by the Navier-Stokes equations. *SIAM Review* **32**, 355.

- DEVILLE, M. O., FISCHER, P. F. & MUND, E. H. 2002 *High-Order Methods for Incompressible Fluid Flow*. Cambridge: Cambridge University Press.
- DZIUK, G. 1991 An algorithm for evolutionary surfaces. *Numer. Math.* **58**, 603.
- FINLAYSON, B. A. 1972 *The Method of Weighted Residuals and Variational Principles. Mathematics in Science and Engineering* 87. New York: Academic Press.
- GUTTENBERG, Z., RATHGEBER, A., KELLER, S., RÄDLER, J. O., WIXFORTH, A., KOSTUR, M., SCHINDLER, M. & TALKNER, P. 2004 Flow profiling of a surface-acoustic-wave nanopump. *Phys. Rev. E* **70**, 056311.
- GUVEN, J. 2004 Membrane geometry with auxiliary variables and quadratic constraints. *J. Phys. A: Math. Gen.* **37**, L313.
- KIRK, B. S., PETERSON, J. W., STOGNER, R. & PETERSEN, S. 2004 *libMesh* – a C++ finite element library, ver. 0.4.3. Available at <http://libmesh.sourceforge.net>.
- KISTLER, S. F. & SCRIVEN, L. E. 1983 Coating flows. In *Computational analysis of polymer processing* (ed. J. R. A. Pearson), chap. 8. Barking, Essex: Applied Science Publishers.
- KOSTUR, M., SCHINDLER, M., TALKNER, P. & HÄNGGI, P. 2005 Chiral separation in microflows. *Phys. Rev. Lett.* (**accepted**).
- LANDAU, L. D. & LIFSHITZ, E. M. 1966 *Hydrodynamik*. Berlin: Akademie Verlag.
- LUO, H. & BEWLEY, T. R. 2004 On the contravariant form of the Navier–Stokes equations in time-dependent curvilinear coordinate systems. *J. Comput. Phys.* **199**, 355.
- NYBORG, W. M. 1965 Acoustic streaming. *Physical Acoustics* **2B**, 265.
- POPINET, S. & ZALESKI, S. 1999 A front-tracking algorithm for accurate representation of surface tension. *Int. J. Numer. Meth. Fluids* **30**, 775.
- RENARDY, Y. & RENARDY, M. 2002 PROST: A parabolic reconstruction of surface tension for the volume-of-fluid method. *J. Comput. Phys.* **183**, 400.
- SAITO, H. & SCRIVEN, L. E. 1981 Study of coating flow by the finite element method. *J. Comput. Phys.* **42**, 53.
- SCRIVEN, L. E. 1960 Dynamics of a fluid interface. Equation of motion for Newtonian surface fluids. *Chem. Eng. Sci.* **12**, 98.
- SEIFERT, U. 1997 Configurations of fluid membranes and vesicles. *Adv. Phys.* **46**, 13.
- SQUIRES, T. M. & QUAKE, S. R. 2005 Microfluidics: Fluid physics at the nanoliter scale. *Rev. Mod. Phys.* **77**, 977.
- SRITHARAN, K., STROBL, C. J., SCHNEIDER, M. F., GUTTENBERG, Z. & WIXFORTH, A. 2005 Acoustic mixing at low Reynolds numbers. *Appl. Phys. Lett.* (**submitted**).
- STONE, H. A. & KIM, S. 2001 Microfluidics: Basic issues, applications, and challenges. *AIChE Journal* **47**, 1250.
- STONE, H. A., STROCK, A. D. & AJDARI, A. 2004 Engineering flows in small devices: Microfluidics toward a Lab-on-a-Chip. *Annu. Rev. Fluid Mech* **36**, 381.
- STROBL, C., FROMMELT, T., GUTTENBERG, Z. & WIXFORTH, A. 2005 Particle separation in a SAW driven microfluidic system with continuous flow (to be published).
- STROBL, C. J., SCHÄFLEIN, C., BEIERLEIN, U., EBBECKE, J. & WIXFORTH, A. 2004 Carbon nanotube alignment by surface acoustic waves. *Appl. Phys. Lett.* **85**, 1427.
- THIELE, U. 2003 Open questions and promising new fields in dewetting. *Eur. Phys. J. E* **12**, 409.
- WIXFORTH, A., STROBL, C., GAUER, C., TOEGL, A., SCRIBA, J. & VON GUTTENBERG, Z. 2004 Acoustic manipulation of small droplets. *Anal. Bioanal. Chem.* **379**, 982.